nature communications

Article

https://doi.org/10.1038/s41467-025-62080-7

Self-assembling solid Sb electrode enables high-capacity, low-cost Ca-Sb battery

Received: 13 May 2024

Accepted: 10 July 2025

Published online: 24 July 2025

Check for updates

Sanghyeok Im[1], Peyman Asghari-Rad[1,3], Kelly Elizabeth Varnell[1,3], Alex T. Vai[2], Jianyi Cui[2], Rachael Howland[2], David Bradwell[2] & Hojong Kim[1]

To decarbonize the power grid using renewable technologies without compromising its reliability, low-cost grid-scale energy storage with resilient long-term performance is required. We report a liquid metal battery that achieves high capacity, low electrode costs, and strong cycling performance by replacing the traditional liquid positive electrode with solid particles. The Ca||Sb(*s*) system described herein achieved 318% higher discharge capacity (715 mAh g^{-1} Sb) and 71% lower electrode cost (19.1 $ kWh^{-1}) than the most competitive liquid metal battery chemistries yet published. The remarkable increase in specific capacity results from the self-assembly of a micro-structured electronically connected Sb network at the positive electrode during cycling while the formation of a liquid Ca-Li alloy at the negative electrode mitigates the growth of solid Ca dendrites. We demonstrate minimal capacity fade of the Ca||Sb(*s*) battery over ~4000 full depth-of-discharge cycles and high coulombic (>98.4%) and energy efficiencies (79–84%) at C-rates (C/8–C/10) relevant for daily storage applications coupled with intermittent renewable energy technologies.

The urgent need to decarbonize the electric grid and integrate renewable energy technologies has created unprecedented demand for large-capacity energy storage. While storage markets are diverse and need solutions with varying characteristics, a common thread is that the cost of electricity storage must be low enough to displace more carbon-intensive methods of ensuring grid stability (e.g., natural gas peaker plants)[1–3]. This cost constraint has thus featured prominently in the recent development of liquid metal batteries (LMBs) made from earth-abundant materials which display reliable performance and high current capabilities due to fast liquid-liquid kinetics[4–7]. For example, a Li||Sb-Pb(*l*) LMB achieved a specific capacity of 171 mAh g^{-1} Sb-Pb and an electrode cost of 65 $ kWh^{-1} while successfully demonstrating a long life span with negligible capacity fade at 500 °C[5]. Even as Li-ion battery (LIB) technology has advanced in recent years leading to lower battery cell costs (50–145 $ kWh^{-1})[8–11], the low-cost floor of LMB chemistries suggests that they could be a cost-effective contributor to stationary energy storage markets.

Among LMBs, those with calcium-based negative electrodes stand out because low-cost, earth-abundant Ca can be paired with several viable positive electrode materials[2,4,12,13]. Bradwell and then Ouchi et al. first demonstrated the feasibility of Ca-based LMBs using a Ca-Mg||Bi(*l*) cell at 550 °C. However, the use of costly Bi metal and the reported low capacity (90 mAh g^{-1} Bi) resulted in a high energy cost of ~144 $ kWh^{-1} [6,13]. The Ca||Sb couple has been considered one of the most cost-effective electrode pairs since the inception of the LMB due to the high cell voltage (~1.0 V) and low cost of Ca and Sb metals[13,14]. Unfortunately, the promise of a Ca||Sb cell has not previously been realized due to the constraint of a liquid positive electrode in traditional LMBs, which necessitates an operating temperature of ~700 °C based on the melting point of Sb ($T_{m,\,Sb}$ = 631 °C). Furthermore, the limited solubility of Ca in liquid Sb (~25 at% Ca) results in a low specific capacity of 136 mAh g^{-1} Sb and a relatively high projected electrode cost of 90 $ kWh^{-1}[14].

We present a recent advancement in LMB technology by pairing a Ca-based liquid metal negative electrode with a solid Sb positive

[1]Materials Science and Engineering, The Pennsylvania State University, University Park, PA, USA. [2]Ambri Incorporated, Marlborough, MA, USA. [3]These authors contributed equally: Peyman Asghari-Rad, Kelly Elizabeth Varnell. e-mail: huk29@psu.edu

electrode to achieve high capacity and low energy cost in a LMB. While it might be assumed that the relative slowness of diffusion in a solid electrode could reduce battery performance compared to a liquid electrode, the features observed and described herein for the Ca||Sb(*s*) system circumvent this logic. This battery operates at ~520 °C in a eutectic $CaCl_2$-LiCl electrolyte (35–65 mol%, or 58.5–41.5 wt%, T_m = 485 °C)[15] which was chosen to allow direct comparison of cycling performance with prior studies of Ca-based LMBs.

Results

High discharge capacity of solid Sb

Figure 1a displays the discharge potential of an Sb electrode (vs. Ca metal) starting from monolithic Sb under constant current (25 mA), showing that a high, useful potential is maintained to a specific capacity beyond 700 mAh g^{-1} Sb. Ex situ analysis of Sb electrodes at various stages of discharge indicates that the initial monolithic Sb transforms into fine particles with cycling (Fig. 1b). Chemical analysis of the products at 160 mAh g^{-1} Sb suggests that the positive electrode is fragmenting due to volume expansion from the progressive formation of Ca-Sb compounds, including $CaSb_2$ and $Ca_{11}Sb_{10}$. We postulate that the high capacity achieved here is due to the fragmentation of Sb which increases surface area and generates short mass transport pathways to allow operation beyond the typical kinetic limitations of solids.

Furthermore, Fig. 1c is a scanning electron microscope (SEM) image of the Sb positive electrode in a Ca||Sb(*s*) cell stopped in a fully charged state after ~1100 cycles and ~12,000 h of run time. The morphology of the Sb positive electrode in this state of charge, consisting of a porous network of micron-scale particles, was preserved by repeatedly immersing the electrode in clean water to remove the electrolyte with minimal agitation. As the operating temperature of the battery is an appreciable fraction of the melting point of antimony, there is likely an ongoing balance between particle fragmentation and sintering over the course of cycling that spontaneously produces this interconnected structure. The self-assembly of a networked Sb electrode structure is likely to increase the electronic connectivity of the electrode to help achieve practical high capacity operation.

The equilibrium potential (E_{eq}) of a particulate Sb electrode during discharge is displayed in Fig. 1d as a function of capacity and mole fraction (x_{Ca}). These data are obtained from the steady open-circuit potential achieved following sequential coulometric titration at a constant current (20 mA). The particulate Sb electrode demonstrated a useful specific capacity as high as 738 mAh g^{-1} Sb by sustaining a high potential (E_{eq} > 0.87 V) until relatively deep states of discharge (x_{Ca} = 0.63), far surpassing the solubility-limited capacity of the Ca||Sb(*l*) couple even at higher temperatures (i.e., 136 mAh g^{-1} Sb at 700 °C)[14]. The high capacity achieved using particulate Sb electrodes is corroborated by electromotive force (emf) measurements of binary Ca-Sb alloys in two-phase regions, as carried out in previous works using a solid CaF_2 electrolyte[16] and in this work using a eutectic $CaCl_2$-LiCl liquid electrolyte (Fig. 1e), which indicate a thermodynamically limited specific capacity of 733 mAh g^{-1} Sb (i.e., 62.5 at% Ca in Sb). Despite the close agreement of the specific capacities determined from the measurement of E_{eq} through coulometric titration and the emf of binary Ca-Sb alloys, the two measurements deviate above

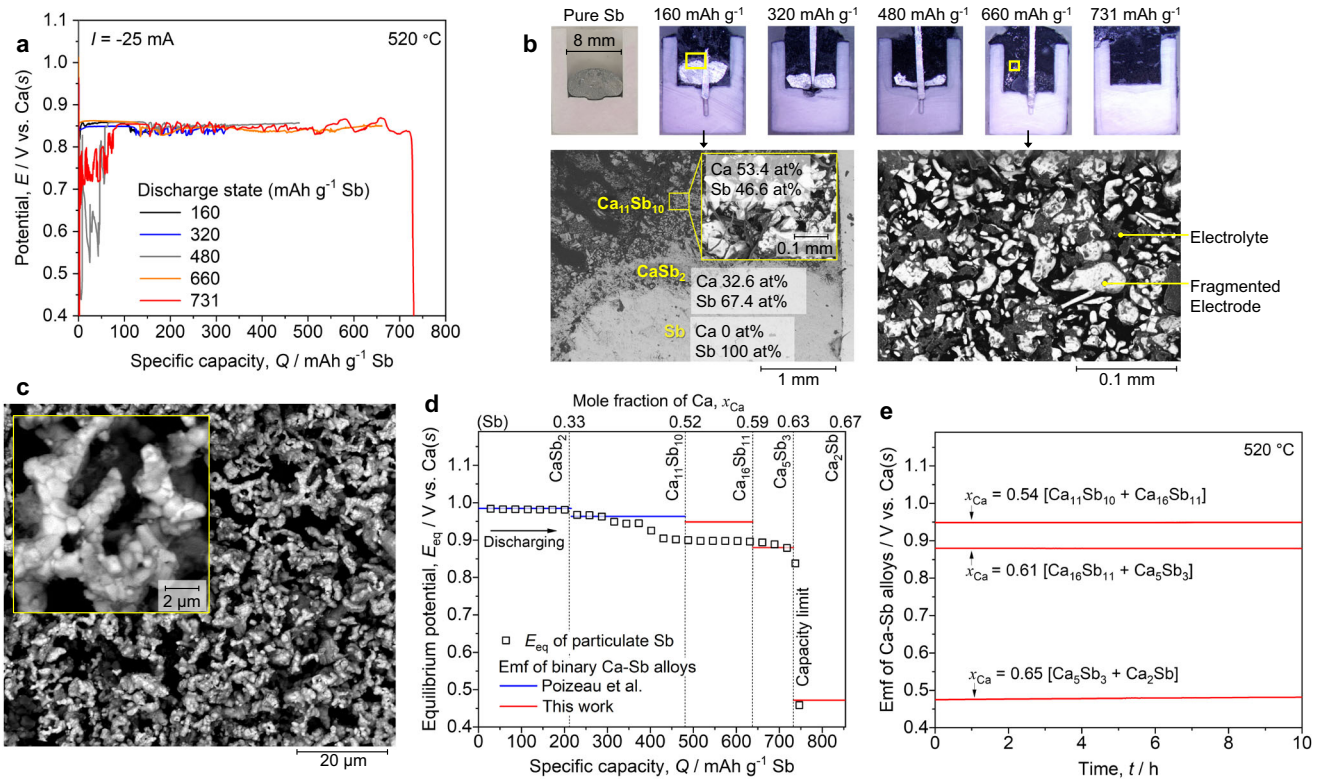

Fig. 1 | Fragmentation of solid Sb and resulting high capacity. a Discharge potential of monolithic Sb electrodes in a three-electrode cell discharged to 160, 320, 480, 660, and 731 mAh g^{-1} Sb, respectively, using constant current (25 mA) in $CaCl_2$-LiCl electrolyte at 520 °C. **b** Optical cross-section images of monolithic Sb electrodes at each state of discharge targeted in (**a**), and electron microscopy images at 160 and 660 mAh g^{-1} Sb, showing the fragmentation of Sb with the formation of Ca-Sb compounds based on EDS point analysis. **c** SEM images of the desalted Sb positive electrode in a fully charged state after ~1100 discharge/charge cycles, primarily at a rate of C/5 between 0.6 and 1.3 V, showing a porous, networked structure consisting of micron-scale positive electrode particles. **d** Equilibrium potential of particulate Sb (square symbols) as a function of specific capacity via coulometric titration compared to the emf of binary Ca-Sb alloys (solid lines) using a liquid $CaCl_2$-LiCl electrolyte (red) in this work or a solid CaF_2 electrolyte (blue)[16] in previous works. **e** Emf measurements of binary Ca-Sb alloys (54–65 at% Ca) in a liquid $CaCl_2$-LiCl electrolyte. These results were replicated in two additional and identical three-electrode cell assemblies.

https://doi.org/10.1038/s41467-025-62080-7

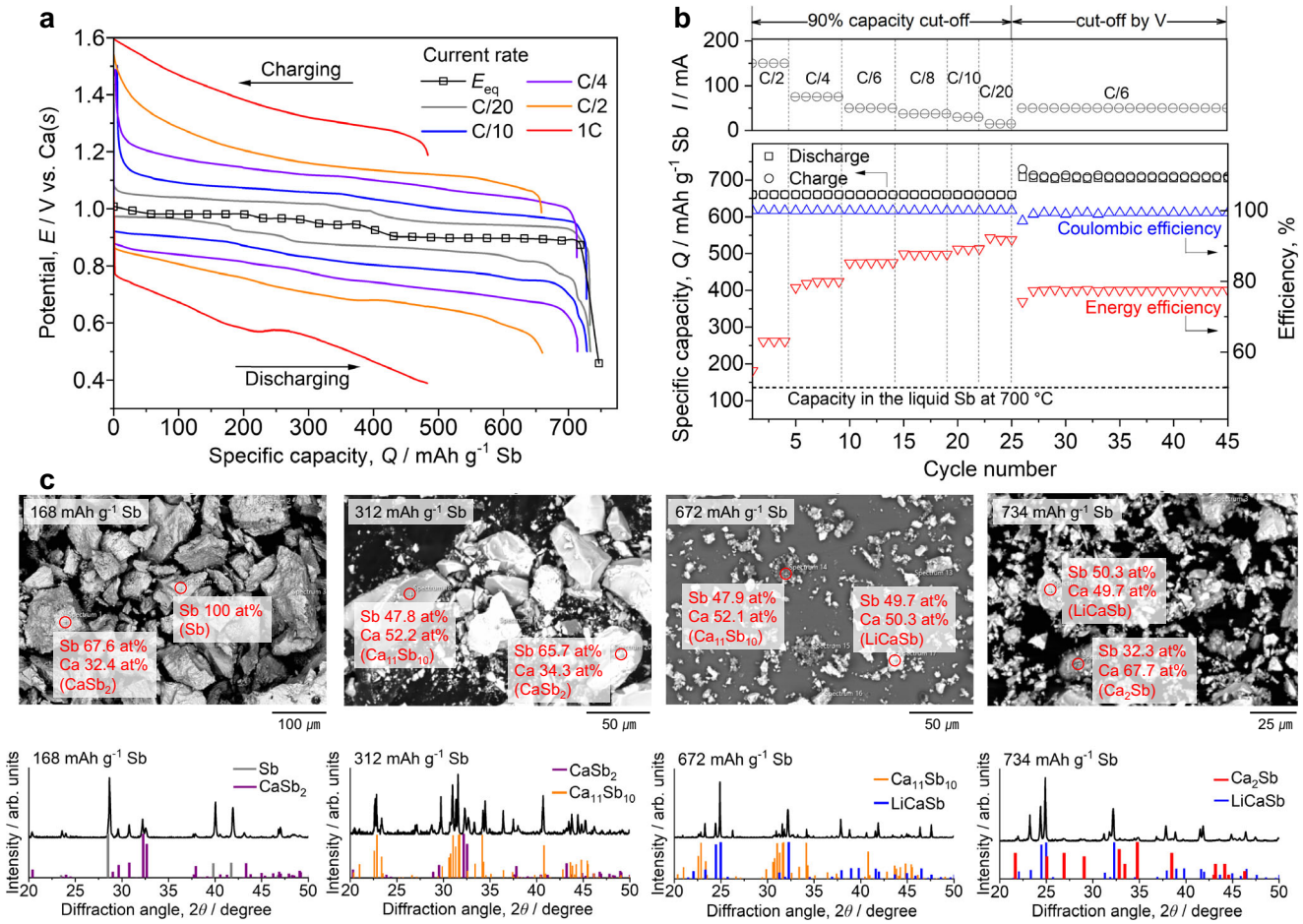

Fig. 2 | Electrochemical performance and characterization of the particulate Sb electrode. a Potentials for a particulate Sb electrode in a SS holder in a three-electrode cell with a eutectic $CaCl_2$-LiCl electrolyte at 520 °C during charging/discharging cycles at various C-rates (25–500 mA, $A = 0.50$ cm^2), in comparison with the equilibrium potential (E_{eq}) determined in Fig. 1d. **b** Specific charge/discharge capacity, coulombic efficiency, and energy efficiency as a function of cycle number at various C-rates for an Sb electrode. These measurements were replicated three times with similar results. **c** SEM images, EDS analysis, and XRD patterns of Sb electrodes after 10 discharge/charge cycles to each respective state of discharge under a constant current rate of C/6.

320 mAh g^{-1} Sb (Fig. 1d) which can be explained by phase analysis of the electrode as summarized in Fig. 2 and discussed further below.

Electrochemical performance of the Sb positive electrode

To observe practical cycling performance compared to the emf measurements discussed above and provide larger positive electrode samples for detailed analysis, a three-electrode electrochemical cell was constructed for the Ca||Sb(*s*) system. Figure 2a, b display cycling performance for a particulate Sb electrode held in a stainless steel (SS) crucible subjected to constant currents equivalent to C-rates of C/20–1 C (based on a theoretical capacity of 733 mAh g^{-1} Sb) and current densities of 50–1000 mA cm^{-2} (based on the macroscopic area of the exposed positive electrode surface, $A = 0.50$ cm^2). This current density is far greater than that typically demonstrated in room temperature Li-ion batteries (<10 mA cm^{-2})[17], consistent with the generally facile kinetics of LMBs. The achieved discharge capacity was more than 659 mAh g^{-1} Sb (>90% of theoretical capacity) at C/20–C/2 rates and was about 400 mAh g^{-1} Sb at the highest 1 C rate, demonstrating a far greater specific capacity for Ca||Sb(*s*) at 520 °C than the Ca||Sb(*l*) couple at 700 °C (<136 mAh g^{-1} Sb) or advanced LIBs (<250 mAh g^{-1})[14,18]. The Sb electrode performance in this cell was reliable with negligible capacity loss over 50 cycles (>30 days) and high round-trip coulombic efficiencies (> 99.4%) during steady state operation at 90–100% of the theoretical capacity. Based on linear current-potential (*I-E*) behavior and impedance spectra, the estimated resistances of the Sb positive electrode remained steady at various states of discharge indicating stable electrical connectivity throughout the positive electrode (Fig. S4). At practical daily cycle rates (C/8–C/10), the calculated energy efficiency is 79–84%, demonstrating utility for grid-scale energy storage when coupled with intermittent renewable energy technologies.

Figure 2c reveals the dynamic phase evolution of the Sb(*s*) electrode through SEM-EDS and X-ray diffraction (XRD) analysis of four particulate Sb electrodes. Each electrode was cycled 10 times to one respective discharge state (i.e., 168, 312, 672, or 734 mAh g^{-1} Sb) at a rate of C/6 before being cooled to room temperature for ex situ analysis. XRD analysis indicates the formation of [Sb + $CaSb_2$] compounds at 168 mAh g^{-1} Sb and [$CaSb_2$ + $Ca_{11}Sb_{10}$] at 312 mAh g^{-1} Sb, in agreement with the known equilibrium phase behavior of the binary Ca-Sb system[16]. Interestingly, at later stages of discharge, the presence of a ternary LiCaSb compound was evident: [$Ca_{11}Sb_{10}$ + LiCaSb] at 672 mAh g^{-1} Sb and [LiCaSb + Ca_2Sb] at the full depth of discharge (734 mAh g^{-1} Sb). The formation of the LiCaSb compound implies an electrode reaction in which Ca and Li are co-deposited without an associated decrease in electrode potential, particularly at later stages of discharge (>320 mAh g^{-1} Sb). The formation of LiCaSb explains the deviation of E_{eq} from the emf of binary Ca-Sb alloys as shown in Fig. 1d. Chemical analysis via inductively coupled plasma-atomic emission

spectroscopy (ICP-AES) corroborates that the discharge reaction is dominated by Ca deposition at early stages and by co-deposition of Ca and Li at later stages of discharge (Table 1).

Cycling performance of the Ca||Sb(*s*) battery

Figure 3a schematically illustrates a Ca | $CaCl_2$-LiCl | Sb(*s*) battery constructed to demonstrate practical implementation of this system. Pure Ca metal was pre-embedded in an iron foam current collector by wetting the foam in molten Ca. The cycling performance of the Ca||Sb(*s*) battery was evaluated at 520 °C using a C/2 current rate, shown in Fig. 3b, c. The Ca||Sb(*s*) battery consistently achieved a high average discharge capacity of 715 mAh g^{-1} Sb (97% of the theoretical capacity) and an average discharge energy of 620 Wh kg^{-1} Sb. Following cell operation for 16 days and over 100 cycles, there was no indication of capacity loss with high coulombic (98.4%) and energy (86%) efficiencies. In addition, the Ca||Sb(*s*) battery with a low electrolyte mass (13 g) achieved 98% coulombic and 80% energy efficiencies using a C/4 current rate (Fig. S5), demonstrating that this battery functions properly with a substantial reduction in electrolyte volume (Figs. S5–S6).

Table 1 | Chemical compositions of Sb positive electrodes after 10 discharge/charge cycles to each respective state of discharge under a constant current rate of C/6 by ICP-AES and ion chromatography (IC) for chloride anion concentrations

State of discharge(mAh g^{-1} Sb)	Concentration (at%)						
	Ca	Li	Sb	Cr	Fe	Ni	Cl
168	27.60	0.010	bal.	-	0.033	-	0.026
312	41.44	0.027	bal.	-	0.008	-	0.029
672	36.18	30.18	bal.	0.001	0.016	-	0.035
734	34.01	35.05	bal.	-	0.025	-	-

Electrochemical formation of the liquid Ca-Li alloy negative electrode

Historically, the use of Ca metal in molten salt electrolytes has presented unpleasant challenges due to its high reactivity and solubility in molten salts, which typically leads to poor coulombic efficiency (< 82%) and rapid cell degradation[19,20]. Furthermore, cell operation at 520 °C, below the melting point of calcium, introduces the possibility of dendritic growth of solid Ca during charging which may result in a short circuit between electrodes or unstable voltage. We report that the excellent cycling performance and absence of erratic behavior observed for this Ca||Sb(*s*) battery can be attributed to the electrochemical formation of a Ca-Li alloy at the negative electrode via co-deposition. Figure 4a displays an ex situ image of a fully charged negative electrode after 100 cycles, showing sound retention of negative electrode materials within the foam current collector. Chemical analysis by ICP-AES in Table 2 confirms that the negative electrode material is a binary Ca-Li (~41 at%, or 11 wt% Li) alloy and XRD analysis (Fig. 4b) corroborates the presence of the Ca(*s*) and Li_2Ca phases with a hypo-eutectic microstructure (L → L + Ca → Ca + Li_2Ca) as observed via SEM (Fig. 4c)[21]. Notably, the formation of this binary Ca-Li

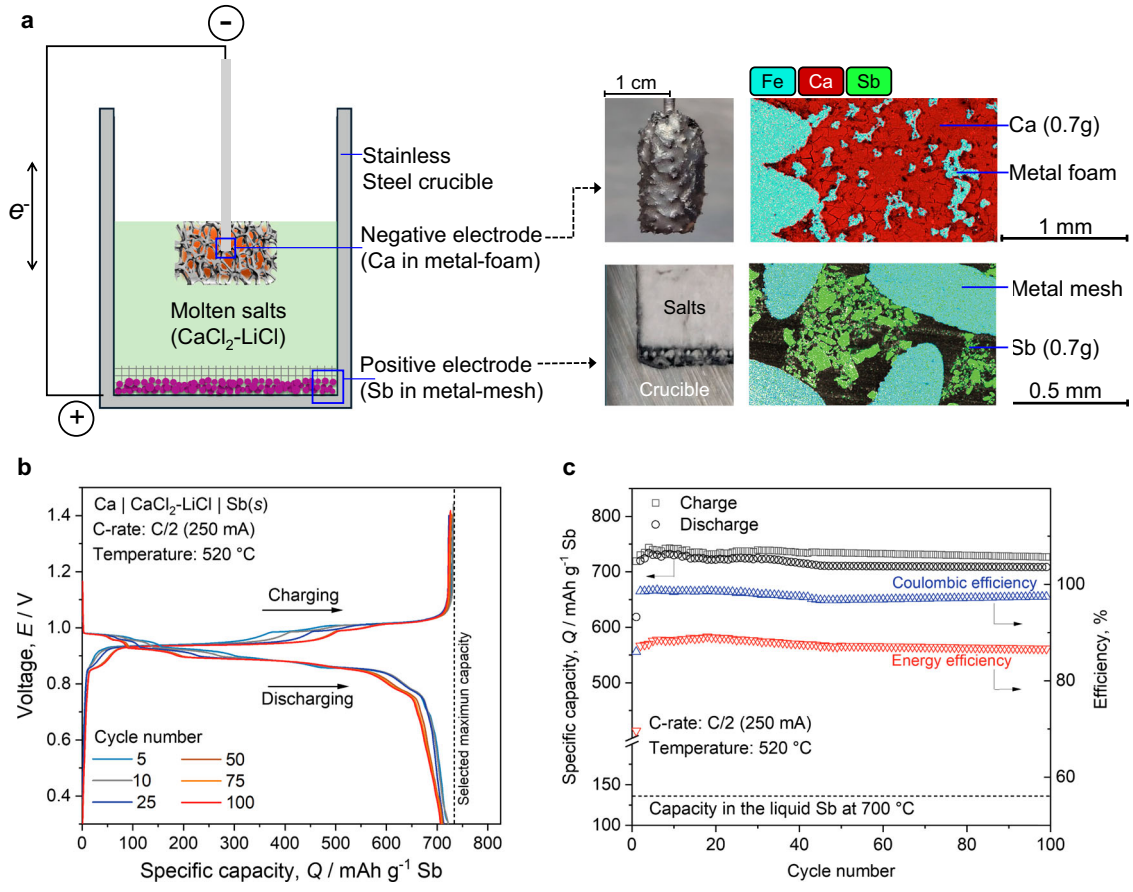

Fig. 3 | Demonstration and performance of a Ca|$CaCl_2$-LiCl|Sb(*s*) battery. **a** Schematic of a Ca||Sb(*s*) battery with optical and elemental X-ray mapping images of the initial configuration for the Ca negative electrode (0.70 g) and Sb positive electrode (0.70 g). **b** Representative cell voltage profiles for 100 charge/discharge cycles operated at a rate of C/2 (250 mA) at 520 °C in the electrolyte (120 g). **c** Specific charge/discharge capacity, coulombic efficiency, and energy efficiency as a function of cycle number. These results were replicated in an additional and identical cell assembly.

https://doi.org/10.1038/s41467-025-62080-7

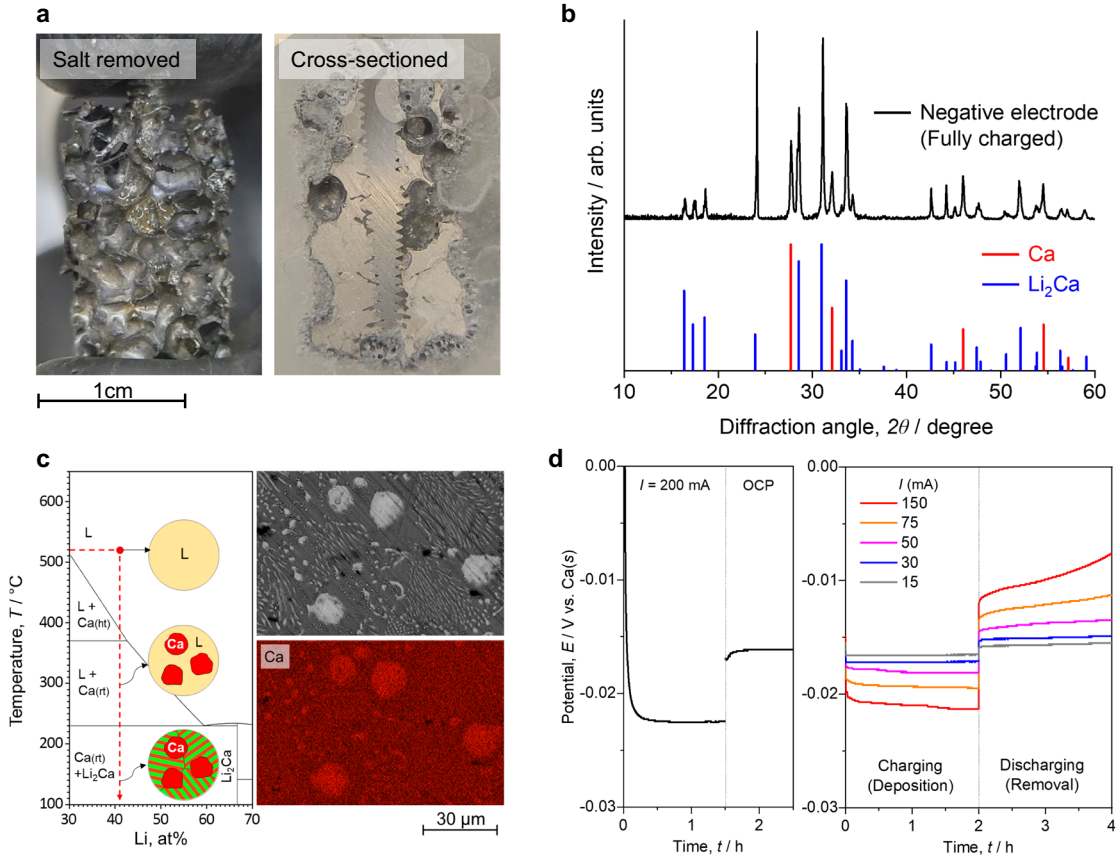

Fig. 4 | Ex situ characterization and kinetics of the liquid Ca alloy negative electrode. a Optical images showing the absence of dendrite formation on the fully charged negative electrode after 100 charge/discharge cycles (Fig. 3) after the salt layer was removed via soaking in dimethyl sulfoxide (left) and after cross-sectioning (right). **b** XRD patterns of the negative electrode indicating the presence of a Ca-Li alloy identified as the Li_2Ca phase. **c** SEM image and Ca element EDS mapping of the negative electrode indicating hypo-eutectic reaction[21]. **d** Overpotentials at the liquid Ca alloy in a three-electrode cell during charging/discharging cycles at various current rates (15–150 mA). The measurement results were obtained from a single three-electrode cell assembly.

Table 2 | ICP-AES chemical composition analysis of the fully charged negative electrode after 100 charge/discharge cycles (Fig. 3)

Sample	Concentration					
	Ca (at %)	Li	Sb	Cr (ppm)	Fe	Ni
#1	57.7	41.3	0.9	246	570	1332
#2	57.8	41.5	0.6	216	403	2091

alloy means that the negative electrode is liquid during operation, which eliminates the chance of solid dendrite growth and reduces the chemical reactivity of Ca. Furthermore, the liquid Ca-Li alloy exhibited remarkably low overpotentials (<10 mV) owing to facile liquid-liquid interfacial reactions and rapid mass transport during cycling at various currents (15–150 mA) as displayed in Fig. 4d.

Long-term cycling stability

As further evidence for the cycling stability achievable with the Ca||Sb(*s*) chemistry, Fig. 5 shows discharge capacity data from a battery over ~4000 cycles and 9 months. This cell was primarily cycled across its full voltage range (0.6–1.2 V) using a high C-rate of C/1.3 at the expense of discharge capacity to demonstrate long-term cycling performance. After an initial set of conditioning cycles, the cell was run under quasi-steady state conditions. Notwithstanding some minor discontinuities in the test data due to an unexpected power outage (partial cool-down), a high coulombic efficiency (>99%) and no net capacity fade are observed even after a number of cycles equivalent to over a decade of daily cycling. A gradual increase in round-trip energy efficiency can also be observed as this test progressed. The increase in steady-state capacity observed after the period of deeper discharge cycles (black square symbol), in which the cell voltage was floated at 0.6 V for 0.5 h in a fully discharged state, further supports the hypothesis that increasing positive electrode fragmentation increases accessible cell capacity.

Cost analysis of the Ca||Sb(*s*) cell

Based on the battery performance achieved (Fig. 3) and the cost of electrode materials, the energy cost and density of the Ca||Sb(*s*) battery are estimated at 19.1 $ kWh^{-1} and 402 Wh kg^{-1}, outperforming prior LMBs (65 $ kWh^{-1} and 194 Wh kg^{-1})[5,7,22,23] by fully utilizing the low-cost particulate Sb positive electrode up to the thermodynamic limit. However, a large volume of electrolyte in this work results in much higher energy cost (236–1956 $ kWh^{-1}), requiring further development of a compact cell design to minimize electrolyte volume (Table S2). Further cost calculations, assuming compact cell assembly with an interelectrode spacing of 0.5 cm (Table S3), indicate that the energy cost can be as low as 34.2 $ kWh^{-1} when factoring in all active components (electrodes and electrolyte) and 46.8 $ kWh^{-1} at a cell level with the addition of a cell case (304 SS). While preliminary cost calculations indicate the advantageous low-cost of the Ca||Sb(*s*) battery for energy storage applications, they also suggest pathways for further cost reduction such as the development of low-cost electrolytes with reduced LiCl content and a compact cell stack to reduce the mass of both electrolyte and inactive cell components.

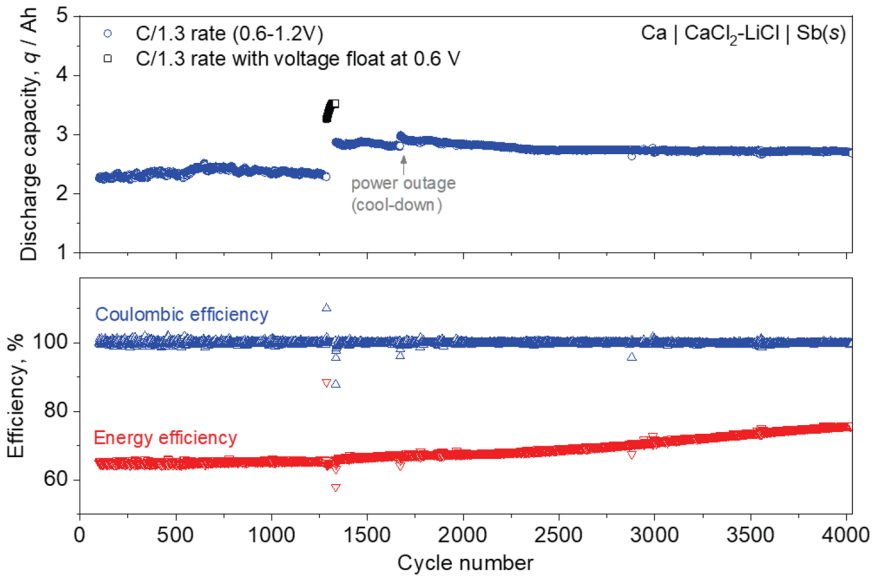

Fig. 5 | Long-term cycles of a Ca|$CaCl_2$-LiCl|Sb(*s*) battery. Discharge capacity, coulombic efficiency, and cycle energy efficiency of a battery operated over 4000 discharge-charge cycles between 0.6 and 1.2 V at a nominal rate of C/1.3 (4 A, ~200 mA cm^{-2}) over ~9 months. Data represented with a black square symbol indicates the discharge capacity obtained with the addition of a constant voltage float of 0.6 V for 0.5 h in a state of full discharge, which resulted in a steady increased capacity in the following cycles. The cell was constructed using 7.0 g of Sb as the positive electrode, 3.3 g of Ca as the negative electrode, and 602 g of the electrolyte and was operated at 520 °C. The measurement results were obtained from a single cell which was sealed and operated under ambient atmospheric conditions.

In conclusion, we demonstrate that the high capacity of the Ca||Sb(*s*) couple in a molten $CaCl_2$-LiCl electrolyte is enabled by spontaneous fragmentation of Sb during cycling, the self-assembly of a porous, electronically conductive positive electrode network, and the formation of a ternary LiCaSb compound without a corresponding loss in cell voltage. Furthermore, in this electrolyte, the formation of a liquid Ca-Li alloy negative electrode allows for rapid electrode kinetics and stable cycling. These findings allowed the successful construction and operation of high-capacity Ca||Sb(*s*) batteries with high efficiency and excellent cycle life under laboratory conditions. While preliminary performance results and cost projections show some potential for this chemistry to be cost competitive based solely on raw materials cost, it is currently unknown if it will be cost-effective at scale, due to unproven performance in a real prototype (as the current cell designs are not suitable for scale up) and the complexity of calculating all associated costs with R&D and manufacturing at scale, requiring further investigation, currently underway at Ambri Inc. These issues make a comparison with the state-of-the-art, such as pumped storage hydropower or lithium-ion batteries, impractical at this stage. Assessing performance will first require designing a more suitable electrolyte, realizing a sealed prototype with realistic and cost-effective electrolyte quantity and chemistry, verifying the real performance in terms of cycle life without excess electrolyte, realizing large scale prototypes, and performing an extensive technoeconomic analysis, currently out of scope of the current publication. The high cost and electrolyte fraction of LiCl in this system present still further opportunities for cost reduction through the design and testing of low-melting, multi-component electrolytes with minimized LiCl content. These results are a foundation for continued development of this system to advance its potential for implementation as an energy storage system as part of a decarbonized electrical grid.

Methods

Cell components and configuration

All cell components were prepared and assembled in an inert Ar-filled glovebox (O_2 < 0.5 ppm). Eutectic $CaCl_2$-LiCl (35-65 mol%) electrolyte was prepared by mixing appropriate weights of anhydrous LiCl (>99.0%, industrial grade) and $CaCl_2$ (>98.0%, industrial grade) in a quartz crucible and pre-melting under the following temperature profile: 8 h at 100 °C and 270 °C for vacuum-drying of salt, 8 h at 430 °C during which time the chamber was purged with Ar gas (99.999%, Praxair), and 700 °C for 3 h to pre-melt the salt. The pre-melted electrolyte was then crushed into fine powder for electrochemical measurements.

Electrode materials were prepared using pure Sb (99.95%, Alfa Aesar) and Ca (99.5%, Alfa Aesar) metals. Monolithic Sb electrodes (Fig. 1a) were prepared by induction melting (IH15A-2 T, Across International) in a BN (99%, Advalue Technology) crucible (8 mm ID, 12 mm OD, 12 mm height), while particulate Sb electrodes were prepared by grinding Sb with a mortar and pestle before loading into a SS crucible (8 mm ID, 12 mm OD, 12 mm height) covered with SS meshes (100 × 100). Porous metal structures, such as 95% porosity iron foam, were prepared as electrode holders for any materials deposited to evaluate negative electrode performance (Fig. 4).

The potential of each Sb working electrode (WE) was measured in a three-electrode cell comprised of a Ca-Bi alloy (x_{Ca} = 0.40) as the reference electrode (RE) and a Ca-Sb alloy (x_{Ca} = 0.40) as the counter electrode (CE). The Ca alloy electrodes were fabricated from pure metals of Ca, Sb, and Bi (99.999%, Sigma-Aldrich) using an arc-melter (MAM-1, Edmund Bühler GmbH). The Ca-Bi RE (2 g) was placed in a BN crucible (8 mm ID, 12 mm OD, 25 mm height) with two capillary holes (1.5 mm) drilled just above the bottom of the crucible and its emf value, 0.801 V vs. Ca(*s*) at 520 °C[24], was used to report the measured electrode potentials versus Ca(*s*). The Ca-Sb CE (15 g) was placed in a large surface area BN crucible (21 mm ID, 25 mm OD, 12 mm height). Both RE and CE alloys were remelted in BN crucibles using an induction heater, and tungsten electrical leads were inserted into the alloys while still molten. The components and configuration of the three-electrode cells used in this study are summarized in Fig. S1 and Table S1.

Electrochemical measurements

The equilibrium potential of particulate Sb (Fig. 1d) was determined by the coulometric titration technique. The Sb was discharged using a constant current of 20 mA for 30 min in each titration step, followed

by a 2 h open-circuit potential measurement to allow for stabilization of the Sb electrode (Fig. S2). For emf measurements of binary Ca-Sb alloys (Fig. 1e), arc-melted alloys (x_{Ca} = 0.54–0.65) were equilibrated by annealing at 650 °C for 72 h after which the equilibrium phases were confirmed by XRD (Fig. S3). The annealed Ca-Sb alloys were placed in BN crucibles with the same dimensions as the RE crucible described above, before their potentials were measured with respect to the Ca-Bi RE for 10 h at 520 °C. All three-electrode cell measurements were validated using additional electrodes in the same cell or in separate cells.

In the two-electrode Ca||Sb(*s*) battery cell of Fig. 3, the Ca negative electrode was fabricated by immersing iron foam (95% porosity) in molten Ca while the particulate Sb positive electrode was prepared in a SS crucible with a SS mesh (40×40) spot welded to the top. Both electrodes were then assembled in a SS crucible with an interelectrode distance of 0.5 cm. Once assembled, pre-melted electrolyte powder (120 g) was poured into the crucible. Detailed descriptions of cell components are summarized in Table S2, including a battery cell with a low mass of electrolyte (13 g) in Fig. S5. The Ca|$CaCl_2$-LiCl|Sb(*s*) battery was placed in an air-tight SS test chamber under an argon atmosphere and cyclically discharged and charged at 520 °C. Electrochemical measurements were carried out using a potentiostat (Interface 5000E, Gamry Instruments) and cell temperature was monitored using a data acquisition system (NI 9211, National Instruments). To confirm observed cell performance, the lab-scale battery cell performance was replicated at least two times in separate cell assemblies. Before each measurement, the cell was subjected to two conditioning cycles under a constant rate of C/4.

For the characterization of cycle life data (Fig. 5), a two-electrode Ca||Sb(*s*) battery cell was prepared and cycled using an Arbin Instruments battery tester for both electrochemical control and data logging. This cell consisted of a SS housing sealed with welds and a brazed ceramic to ensure electrical isolation between the positive and negative terminals. Internally, the liquid negative electrode was held within a stack of SS meshes (35 mesh) with a macroscopic area of ~19.7 cm^2. The positive electrode was contained in a SS crucible with an opening of equal area covered with SS mesh (80 × 700 Dutch weave). The electrode holding components were assembled facing each other in a prismatic configuration at a nominal interelectrode spacing of 1.3 cm. Molten electrolyte was then poured into the housing around the electrode assemblies and allowed to freeze before the cell was sealed. Further construction details for this cell are summarized in Table S2. This cell was initially subjected to ~30 conditioning cycles before being switched to high-rate (C/1.3) quasi-steady state cycles that were the main subject of the test. As the sealed cell was operated in open air at ambient conditions, lower C-rate (C/12–C/4) conditioning cycles and several potentiostatic holds were used to both condition the electrodes and validate that the physical cell construction, casing, and seal were sound before long-term cycle testing began.

Ex situ characterization/analysis

Upon completion of electrochemical measurements, the electrodes were raised above the electrolyte and the cell was cooled to room temperature. Each electrode was separated from the cell assembly and immersed in dimethyl sulfoxide (99.9%, Sigma-Aldrich) inside of the glovebox for 3 days to remove the entrained salt layer. The electrode was then removed from the glovebox and mounted in epoxy resin before being cross sectioned using a low speed saw. One half of the cross sectioned electrode was polished with 1200-grit sandpaper (<15 min) using isopropyl alcohol (99.5%, Sigma-Aldrich) while the electrode material was separated from the second half of the cross sectioned electrode by removing the current collectors/holders (<15 min). Following this sample preparation under ambient conditions, cross sectioned electrodes were immediately transferred to a glovebox, sealed in a glass ampoule, and stored under an Ar atmosphere. The sealed ampoule was transported and opened directly before ex situ characterization to minimize the exposure of the prepared samples to ambient conditions (<5 min). The polished sample was used for microstructural characterization using SEM (FEI Quanta 200) coupled with energy dispersive spectroscopy (EDS) and the separated electrode material was used for phase analysis by XRD (PANalytical Empyrean, Cu Kα-radiation) or chemical analysis by ICP-AES (Thermo iCAP 7400). For characterization of Sb electrodes in a fully charged state (Fig. 1c), multiple changes of deionized water were used over several days to remove salt and reveal the electrode morphology under ambient conditions.

Cost analysis

The electrode materials cost per unit energy, C, was calculated using $C = \sum_i P_i m_i / E_D$, where P_i is the commodity bulk price of each electrode material in \$ kg^{-1}, m_i is the mass in g, and E_D is the average discharge energy in kWh. A detailed cost calculation for the Ca||Sb(*s*) battery is presented in Table S3 based on electrochemical performance (Fig. 3). This approach for electrode cost calculation is consistent with the previously reported values for various LMB cells and the estimated values are compared in Table S4. The cost calculations for the Ca||Sb(*s*) battery were extended to include the mass of electrolyte assuming an interelectrode distance of 0.5 cm, a macroscopic electrode surface area of 1 cm^2, and the liquid-state density of each salt at 520 °C. Finally, the mass of the cell case (304 SS) needed for the cell assembly was included to estimate the cell-level cost for a Ca||Sb(*s*) battery.

Data availability

All data generated or analyzed in this study are provided in the Supplementary Information/Data files. Source data are provided with this paper.

References

1. Gür, T. M. Review of electrical energy storage technologies, materials and systems: challenges and prospects for large-scale grid storage. *Energy Environ. Sci.* **11**, 2696–2767 (2018).
2. Vesborg, P. C. K. & Jaramillo, T. F. Addressing the terawatt challenge: scalability in the supply of chemical elements for renewable energy. *RSC Adv.* **2**, 7933–7947 (2012).
3. Dunn, B., Kamath, H. & Tarascon, J. M. Electrical energy storage for the grid: a battery of choices. *Science* **334**, 928–935 (2011).
4. Kim, H. et al. Liquid metal batteries: past, present, and future. *Chem. Rev.* **113**, 2075–2099 (2013).
5. Wang, K. et al. Lithium-antimony-lead liquid metal battery for grid-level energy storage. *Nature* **514**, 348–350 (2014).
6. Ouchi, T., Kim, H., Spatocco, B. L. & Sadoway, D. R. Calcium-based multi-element chemistry for grid-scale electrochemical energy storage. *Nat. Commun.* **7**, 1–5 (2016).
7. Bradwell, D. J., Kim, H., Sirk, A. H. C. & Sadoway, D. R. Magnesium-antimony liquid metal battery for stationary energy storage. *J. Am. Chem. Soc.* **134**, 1895–1897 (2012).
8. Wentker, M., Greenwood, M. & Leker, J. A bottom-up approach to lithium-ion battery cost modeling with a focus on cathode active materials. *Energy* **12**, 1–18 (2019).
9. Mauler, L., Duffner, F., Zeier, W. G. & Leker, J. Battery cost forecasting: a review of methods and results with an outlook to 2050. *Energy Environ. Sci.* **14**, 4712–4739 (2021).
10. Mineral commodity summaries 2023. *Mineral Commodity Summaries* 210, https://pubs.usgs.gov/publication/mcs2023 (2023) https://doi.org/10.3133/mcs2023.
11. Orangi, S. et al. Historical and prospective lithium-ion battery cost trajectories from a bottom-up production modeling perspective. *J. Energy Storage* **76**, 109800 (2024).
12. Calcium Commodity Price. https://www.intratec.us/chemical-markets/calcium-price (2023).

13. Bradwell, D. J. Liquid metal batteries: ambipolar electrolysis and alkaline earth electroalloying cells. Ph.D Thesis. (Massachusetts Institute of Technology, 2011).
14. Ouchi, T., Kim, H., Ning, X. & Sadoway, D. R. Calcium-antimony alloys as electrodes for liquid metal batteries. *J. Electrochem Soc.* **161**, A1898–A1904 (2014).
15. Mahendran, K. H., Nagaraj, S., Sridharan, R. & Gnanasekaran, T. Differential scanning calorimetric studies on the phase diagram of the binary LiCl–$CaCl_2$ system. *J. Alloy. Compd.* **325**, 78–83 (2001).
16. Poizeau, S., Kim, H., Newhouse, J. M., Spatocco, B. L. & Sadoway, D. R. Determination and modeling of the thermodynamic properties of liquid calcium-antimony alloys. *Electrochim. Acta* **76**, 8–15 (2012).
17. Li, H. Practical evaluation of Li-ion batteries. *Joule* **3**, 911–914 (2019).
18. Yan, S. et al. Utilizing in situ alloying reaction to achieve the self-healing, high energy density and cost-effective Li||Sb liquid metal battery. *J. Power Sources* **514**, 1–7 (2021).
19. Takeda, O., Uda, T. & Okabe, T. H. Chapter 2.9 - Rare Earth, Titanium Group Metals, and Reactive Metals Production. in (ed. Seetharaman, S. B. T.-T. On P. M.) 995–1069. https://doi.org/10.1016/B978-0-08-096988-6.00019-5. (Elsevier, 2014).
20. Sharma, R. A. Solubilities of calcium in liquid calcium chloride in equilibrium with calcium-copper alloys. *J. Phys. Chem.* **74**, 3896–3900 (1970).
21. Bale, C. W. & Pelton, A. D. The Ca–Li (Calcium-Lithium) system. *J. Phase Equilibria* **8**, 125–127 (1987).
22. Ning, X. et al. Self-healing Li-Bi liquid metal battery for grid-scale energy storage. *J. Power Sources* **275**, 370–376 (2015).
23. Li, H. et al. Liquid metal electrodes for energy storage batteries. *Adv. Energy Mater.* **6**, 1–19 (2016).
24. Kim, H. et al. Thermodynamic properties of calcium-bismuth alloys determined by emf measurements. *Electrochim. Acta* **60**, 154–162 (2012).

Acknowledgements

This work was supported by Ambri Incorporated (Award No: 250373, HK) and US National Science Foundation (Award No: CBET-1844170, HK). The authors also wish to acknowledge Prof. Donald Sadoway for his mentorship, support, and leadership in advancing the research and development of Liquid Metal Batteries.

Author contributions

S.I. and H.K. conceived the idea for the project. S.I. performed fundamental measurements. P.A. and K.E.V. equally contributed to discussing and drafting the manuscript and supported materials characterization. A.T.V., J.C., R.H., and D.B. contributed to method development, data validation, long-term cycling data acquisition, and manuscript revision. D.B. and H.K. supervised the progress of the project.

Competing interests

The authors declare no competing interests.

Additional information

Supplementary information The online version contains supplementary material available at https://doi.org/10.1038/s41467-025-62080-7.

Correspondence and requests for materials should be addressed to Hojong Kim.

Peer review information *Nature Communications* thanks Junli Xu and the other anonymous reviewers for their contribution to the peer review of this work. A peer review file is available.